Applied Catalysis B: Environmental 202 (2017) 518–527

Contents lists available at ScienceDirect

Applied Catalysis B: Environmental

journal homepage: www.elsevier.com/locate/apcatb

Fabrication of nitrogen doped graphene quantum dots-BiOI/$MnNb_2O_6$ p-n junction photocatalysts with enhanced visible light efficiency in photocatalytic degradation of antibiotics

Ming Yan [a], Yinqun Hua [a], Fangfang Zhu [b], Wei Gu [b], Jinhui Jiang [c], Hongqiang Shen [b], Weidong Shi [b,*]

[a] School of Material Science and Engineering, Jiangsu University, Zhenjiang 212013, China
[b] School of Chemistry and Chemical Engineering, Jiangsu University, Zhenjiang 212013, China
[c] School of Physics, Huazhong University of Science and Technology, Wuhan 430074, China

ARTICLE INFO

Article history:
Received 1 March 2016
Received in revised form 8 August 2016
Accepted 20 September 2016
Available online 20 September 2016

Keywords:
p-n Junction
NGQDs-BiOI/$MnNb_2O_6$
Photocatalysts
Antibiotics

ABSTRACT

Novel p-n junction photocatalysts nitrogen doped graphene quantum dots (NGQDs)-BiOI/$MnNb_2O_6$ have been prepared via hydrothermal method for the environmental remediation. The photocatalytic activity of as-prepared photocatalysts was evaluated by the degradation of different antibiotics such as tetracycline (TC), oxytetracyline, ciprofloxacin and doxycycline. Compared with single $MnNb_2O_6$ and BiOI, the hybrid materials (NGQDs-BiOI/$MnNb_2O_6$) could significantly enhance photocatalytic activity. Meanwhile, both the BiOI/$MnNb_2O_6$ ratio (Bi/Mn ratio) and the amount of NGQDs displayed important influence on the antibiotics degradation. In addition, the 5%NGQDs-Bi/Mn sample performed the optimum photocatalytic degradation toward TC (87.2%) within 60 min. By further studies based on the electron spin resonance (ESR) and active species trapping experiments, this enhanced photocatalytic property could be ascribed to high charge carrier mobility of NGQDs and the p-n junction photocatalytic systems, which greatly promoted efficient separation of charge carriers.

1. Introduction

In the recent years, the elimination of antibiotics from aquatic ecosystem have aroused much interests due to their associated specific environmental risks and impact on environment issues and human health [1,2]. As the high production and usage of drugs in the world, antibiotics are widely applied in the treatment of bacterial infection, easily discharge into the aquatic ecosystem via the wastewater effluent, animal manure and soil erosion [3]. Recent researches have showed that the micropollutants of tetracycline antibiotics at the concentrations were about 4.58 mg kg^{-1}, 86–199 μg kg^{-1} and 0.13–0.51 μg L^{-1} in the animal dung samples, soils and surface waters in the environment, respectively [4,5]. Therefore, it is vital to find an effective method for eliminating the antibiotics from aqueous environments.

Semiconductor photocatalysis, which is considered as a green and sustainable technology, has aroused much interests because of its wide application in water purification and environmental protection by solar energy [6–9]. In order to effectively utilize visible light (48% of the incoming solar energy), lots of visible-light-driven photocatalysts have been prepared successfully, such as g-C_3N_4 [10], Ag_3VO_4 [11], $BiVO_4$ [12], Bi_2WO_6 [13] and other Bi-based photocatalysts [14,15]. Among these semiconductors, BiOI as a p-type bismuth oxyhalides semiconductor, exhibiting excellent photocatalytic activity under visible light irradiation because of its narrow band gap (Eg = 1.63–1.94 eV) [16,17]. However, the photocatalytic activity of single BiOI had been limited by some disadvantages, such as low efficiency of light absorption, slow rate of charge transfer and high recombination probability of the photogenerated electron-hole pairs. Therefore, it is necessary to further improve the photocatalytic activity for practical applications. Up to now, some strategies have been proposed to improve the photocatalytic activity of BiOI, such as modified by noble metals [18,19], constructed the heterojunctions [20,21], induced oxygen defect [22,23] and sensitizer [24]. Meanwhile, it has been proven that the heterostructures between a n-type semiconductor and a p-type semiconductor will greatly facilitate the separation and transfer of charge carriers because of the existence of an internal electric field built at the heterojunction interface, thus highly enhancing the photocatalytic activity.

* Corresponding author.
E-mail addresses: swd1978@ujs.edu.cn, shiwd999@yahoo.com (W. Shi).

http://dx.doi.org/10.1016/j.apcatb.2016.09.039
0926-3373/

On the one hand, $MnNb_2O_6$, as a n-type transition metal niobate photocatalyst, had attracted much attention in photocatalytic applications due to its narrow band energy of 2.2 eV. Hu et al. had reported that the 3D flower-like nanostructure $MnNb_2O_6$ had excellent photocatalytic performance for photodegradation of methylene blue under visible light irradiation [25]. Therefore, it is believed that the p-n junction coupling of BiOI and $MnNb_2O_6$ will exhibit superior performance by efficiently utilizing visible light.

On the other hand, as a novel carbon materials with the size less than 10 nm, graphene quantum dots (GQDs) had been a new direction in current research due to their environmentally friendly, nontoxic degradable, and low-cost features [26–31]. Moreover, when the nitrogen atoms were introduced into the carbon lattice of quantum dots (NGQDs), it can modulate the electronic properties of quantum dots and induce the "activation region" on the GQDs surfaces [32–35]. This kind of activated region can participate in catalytic reactions directly, such as the oxygen reduction reaction [36,37]. Hence, we conceive of introducing the NGQDs into the p-n junction to act an ideal electron mediate and supporter, which extremely facilitate the charge migration and prolong the charge lifetimes by suppressing the recombination of photogenerated electrons and holes.

Based on the above consideration, we reported a novel p-n junction of NGQDs-BiOI/$MnNb_2O_6$ by a simple hydrothermal method. Antibiotics such as tetracycline (TC), oxytetracyline, ciprofloxacin and doxycycline were chosen as target pollutants to explore the photocatalytic performance. Results showed that both the Bi/Mn ratio and NGQDs amount displayed important influence on the photocatalyst activity. Furthermore, tentative mechanism of the enhanced photocatalytic activity was also discussed based on the active species trapping experiments and electron spin resonance (ESR) analysis.

2. Experiment section

2.1. Synthesis of NGQDs

The NGQDs was obtained by directly pyrolyzing $C_6H_5O_7(NH_4)_3$. 1 g $C_6H_5O_7(NH_4)_3$ and 20 mL of H_2O were put into a beaker and heated to 200 °C with an oil bath pan. Within 30 min, the color of the solution slowly became the light orange, implying the formation of NGQDs. Ultimately, a quantity of NaOH (10 mg/mL) solution were added to adjust the pH value of 7 [38].

2.2. Synthesis of $MnNb_2O_6$ nanostructures

Firstly, 0.5 g Nb_2O_5 and 3.37 g KOH were added in the 60 mL of distilled water and then transferred into a 100 mL Teflon-lined stainless steel autoclave at 200 °C for 3 days. After cooling naturally, the clear solution of $[Nb_6O_{19}]^{8-}$ was obtained. Then, the above solution (4 mL) was diluted with 10 mL distilled water. The pH of obtained aqueous solution was adjusted to 7.8 by the addition of HCL solution. After that, 0.035 g $MnCl_2{\cdot}4H_2O$ and 1 g K_2SO_4 were added under continuous stirring for 30 min. Finally, the obtained precursor was transferred into a 50 mL Teflon-lined stainless autoclave at 260 °C for 24 h. The product was filtered, washed with distilled water, and dried in a vacuum at 60 °C for 12 h.

2.3. Preparation of NGQDs-BiOI/$MnNb_2O_6$

Typically, 1 mmol of $Bi(NO_3)_3{\cdot}5H_2O$ was dissolved in 20 mL of ethylene glycol, and X (0.2, 0.33, 1, 3 and 5) mmol $MnNb_2O_6$ was added in above solution with continuous stirring for 30 min. Then, 1 mmol KI was dissolved in this solution and the color of solution became orange. Subsequently, 20 mL of distilled water was slowly dropped to the orange solution, red precipitate was generated gradually (abbreviated as 5Bi/Mn, 3Bi/Mn, Bi/Mn, Bi/3Mn, and Bi/5Mn). After that, different amount of the NGQDs was dissolved in above solution with continuous stirring for 60 min. The preparation of NGQDs-BiOI/$MnNb_2O_6$ with different starting mass ratios of NGQDs to BiOI/$MnNb_2O_6$ (0.01, 0.03, 0.05 0.07 and 0.1) were labeled as 1%NGQDs-BiOI/$MnNb_2O_6$, 3%NGQDs-BiOI/$MnNb_2O_6$, 5%NGQDs-BiOI/$MnNb_2O_6$, 7%NGQDs-BiOI/$MnNb_2O_6$ and 10%NGQDs-BiOI/$MnNb_2O_6$. Finally, the precursor was transferred into a 50 mL Teflon-lined stainless autoclave at 180 °C for 12 h. The obtained precipitate was collected by centrifugation, washed with the deionized water and absolute ethanol for several times, dried at 60 °C for 12 h. For comparison, pure BiOI was prepared with the same method without $MnNb_2O_6$ and NGQDs.

2.4. Characterization

X-ray diffraction (XRD) patterns measurements were undertaken using a D/MAX-2500 diffract meter (Rigaku, Japan) with a nickel-filtered Cu Kα radiation source (λ = 1.54056 Å). The X-ray photoelectron spectroscopy (XPS) was obtained by a Thermo ESCALAB 250X (America) electron spectrometer using 150WAl Ka X-ray sources. The scanning electron microscopy (SEM) was obtained by the Hitachi S-4800 field emission SEM (FESEM, Hitachi, Japan) to observe the morphology of the as-prepared samples. Transmission electron microscopy (TEM), high-resolution transmission electron microscopy (HRTEM) and High angle angular dark field-scanning transmission electron microscopy (HAADF-STEM) were gathered on an F20 S-TWIN electron microscope (Tecnai G2, FEI Co.), equipping with a 200 kV accelerating voltage. The photoluminescence (PL) spectra for solid samples were obtained on a F4500 (Hitachi, Japan) photoluminescence detector. UV–vis absorption spectra (DRS) was collected using a Shimadzu UV–vis 2550 spectrophotometer. Reflectance measurements were performed on powdered samples, $BaSO_4$ was used as a standard reference. The photocurrent and electrochemical impedance spectroscopy (EIS) measurements were conducted by use of a CHI852C electrochemical workstation and a CHI760E workstation, respectively. The ESR signals of radicals spin-trapped by spin-trapreagent 5,5-dimethyl-1-pyrroline N-oxide (DMPO) were examined on a Bruker EPR A 300-10/12 spectrometer.

2.5. Photocatalytic analysis

The photocatalytic activity of as-prepared samples were evaluated by the degradation of antibiotics (TC, oxytetracyline, ciprofloxacin and doxycycline) under visible light in a photochemical apparatus. A 250W xenon lamp with a cut-off filter was used to remove the wavelength less than 420 nm. In details, 50 mg of the sample power was dispersed into the 100 mL solution of antibiotics (10 mg/L), in order to the insure the adsorption equilibrium, the suspension solution was kept stirring for 30 min in darkness before irradiation. At the same irradiation intervals, 6 mL aqueous solution was sampled and separated from the suspended catalyst particles for analysis. The photocatalytic degradation ratio was tested via the intensity changes of the absorption peak at 357 nm, 275 nm, 277 nm and 271 nm to determine the concentration of TC, oxytetracyline, ciprofloxacin and doxycycline at different times by the same UV–vis spectrophotometer (UV-2550, Shimadzu, Japan).

2.6. Photoelectrochemical measurements

Photocurrent tests were carried out in a conventional three electrode system on the CHI852C electrochemical workstation by using 0.5 M Na_2SO_4 electrolyte, and the irradiation area was 1 cm^2 under 150 W xenon lamp. A Pt foil as the counter electrode and an Ag/AgCl

electrode as a reference electrode. The working electrodes were prepared as follows: 0.3 g of the as-prepared sample and 0.01 g Polyvinyl Pyrrolidone (PVP) were dispersed in 3 mL ethanol and 0.03 mL oleic acid to produce a suspension, which was then coated onto a $1.5 \times 3\,cm^2$ FTO glass electrode and annealed at 500 °C in air for 2 h. EIS measurements were carried out in a three electrode electrochemical cell on a CHI760E electrochemical workstation. A 0.1 M KCl solution containing 5 mM $Fe(CN)_6^{3-/4-}$ was used as the electrolyte.

2.7. Active species trapping and ESR experiments

In the active species trapping experiments, 1 mM triethanolamine (TEOA), 1 mM 1,4-benzoquinone (BQ) and 1 mM isopropanol (IPA) were respectively employed as the scavengers for h^+,$^\bullet O_2^-$ and $^\bullet$OH. The method was similar to the former photocatalytic activity test. Furthermore, $^\bullet$OH and $^\bullet O_2^-$ radicals were measured by the ESR technique by the DMPO. Before to determine $^\bullet$OH and $^\bullet O_2^-$ radicals, 10.0 mg sample was dissolved in 0.5 mL deionized water or 0.5 mL methanol, and then 45 μL DMPO was added with ultrasonic dispersion for 5 min, respectively.

3. Results and discussion

3.1. Characterization of the NGQDs

The TEM image of the NGQDs was described in Fig. S1a, it can be clearly observed that the size of the NGQDs was about 5–10 nm. The XPS measurement was also carried out to examine the chemical composition of the as-synthesized NGQDs. Fig. S1b displays the survey spectrum of NGQDs, the three predominant peaks located at 284.1 eV, 400.2 eV and 530.4 eV, which can be ascribed to the C 1s, N 1s and O 1s, respectively. The XPS expanded spectrums of the C1s (Fig. S1c) were observed at 284.6 eV, 285.2 eV, 287.3 eV and 289.0 eV, which corresponded to C—C, C—N, C=O and O—C=O, respectively [38–40]. As shown in Fig. S1d, the N 1s was fitted to four peaks centered at 399.2 eV, 399.8 eV, 401.1 eV and 402.0 eV, which assigned to the pyridinic N, pyrrolic N, quaternary N and N-H, respectively [41,42]. The above XPS analysis clearly confirmed the successful adulteration of nitrogen into the GQDs.

3.2. Characterization of the NGQDs-BiOI/$MnNb_2O_6$

The crystalline phases of the composites were investigated via XRD. As can be seen from Fig. 1a, the pristine BiOI showed a series of sharp diffraction peaks, which can be indexed into the tetragonal phase of BiOI (JCPDS 10-0445). While the $MnNb_2O_6$ can be ascribed to the columbite phase (JCPDS 72-0484) with no observable impurities. With respect to the BiOI/$MnNb_2O_6$ composites, the peak intensity of $MnNb_2O_6$ became stronger with increasing the content of $MnNb_2O_6$. However, the positions of the diffraction peaks remain unchanged for NGQDs-BiOI/$MnNb_2O_6$ samples in Fig. 1b, which means the introduction of the NGQDs does not change the phase structure of BiOI/$MnNb_2O_6$ composites. Moreover, no NGQDs diffraction peak was discovered, which may be due to the small amounts, high dispersion and low crystallinity of NGQDs in the NGQDs-BiOI/$MnNb_2O_6$ heterojunctions.

3.3. Morphology

The morphologies of as-prepared samples were detected by SEM. It can be observed that pure BiOI displayed a large scale of microspheres structures which were consisted of numerous nanosheets in Fig. 2a–b. In Figs. 2c–d, 3D nanostructures $MnNb_2O_6$ exhibited a uniform hexagonal nanoflower structure with excellent dispersion. The morphologies of NGQDs-BiOI/$MnNb_2O_6$ composites were different from that of uniform BiOI microspheres, which suggested that the BiOI nanosheets were mixed with 3D flower-like $MnNb_2O_6$ in Fig. 2e–f. The microstructure of the NGQDs-BiOI/$MnNb_2O_6$ was determined by TEM and HRTEM. As shown in Fig. 3a, the BiOI nanosheets and 3D flower-like $MnNb_2O_6$ were close enough to form an intimate interface, in addition, there were a lot of dark dots with the diameter about 5–10 nm can be seen. This signified that the NGQDs had been anchored on the BiOI/$MnNb_2O_6$ successfully and intimate integration. As shown in Fig. 3b, there were three sets of distinct lattice fringes in the pattern. The interplanar spacing of NGQDs was 0.200 nm, which was consistence with that of the graphite carbon source [33]. Meanwhile, the distinct lattice fringes with spacing of 0.361 nm and 0.167 nm corresponded well to the (002) facet of BiOI and (311) facet of $MnNb_2O_6$, respectively. To further delineate the combination and spatial distribution of BiOI, $MnNb_2O_6$ and NGQDs, the HAADF-STEM was employed. From the pictures with distinct color contrast in Fig. 4, the Bi, I, Mn, Nb, O, C and N elemental maps could be observed, which illustrated that BiOI, $MnNb_2O_6$ and NGQDs were closely contacted with each other.

3.4. UV–vis absorption spectra

The light absorption ability of pure BiOI, $MnNb_2O_6$, Bi/Mn and 5% NGQDs-Bi/Mn samples were investigated by the UV–vis absorption. As described in Fig. 5a, BiOI showed strong absorption in the visible light range with the obvious absorption edge around 670 nm. Meanwhile, it could be found that BiOI was a narrow band gap semiconductor with the band gap is about 1.85 eV (Fig. 5b). While bare $MnNb_2O_6$ had the sharp absorption edge at about 560 nm, which corresponded to the band gap energy of 2.2 eV. The Bi/Mn sample was the mixture of $MnNb_2O_6$ and BiOI in the mole ratio of 1:1, which had a moderate light absorption edge between the $MnNb_2O_6$ and BiOI samples. When the Bi/Mn was decorated with NGQDs, the 5%NGQDs-Bi/Mn sample exhibited enhanced absorption intensity, which may result in the formation of more photogenerated electron-hole pairs. Similar phenomena were also observed by other researchers [43–45].

3.5. XPS analysis

XPS was carried out to analyze the surface chemical compositions of BiOI, $MnNb_2O_6$ and 5% NGQDs-Bi/Mn photocatalysts. The XPS spectrums of BiOI, $MnNb_2O_6$ and 5% NGQDs-Bi/Mn samples in Fig. 6a indicated that Bi, I and O existed on the surface of BiOI, Mn, Nb and O elements were on the surface of $MnNb_2O_6$, and Bi, I, Mn, Nb, O, C and N were all existing in the 5% NGQDs-Bi/Mn sample. Fig. 6b displayed two strong peaks at 158.8 eV and 164.1 eV, which assigned to Bi $4f_{5/2}$ and Bi $4f_{7/2}$ and should originate from BiOI. However, when BiOI combined with $MnNb_2O_6$ and NGQDs, the Bi 4f peaks of 5% NGQDs-Bi/Mn displayed a slight shift toward the high binding energy. Meanwhile, the binding energy of I 3d in the 5% NGQDs-Bi/Mn composites also exhibited a little shift to the high energy region compared to the single BiOI (Fig. 6c). On the other hand, the Mn 2p XPS spectrums for the $MnNb_2O_6$ and 5% NGQDs-Bi/Mn samples were shown in Fig. 6d. For the single $MnNb_2O_6$, the peaks of Mn 2p located at 641.4 eV and 654.3 eV, while these peaks shifted to 640.3 eV and 653.1 eV for the 5% NGQDs-Bi/Mn composites. Correspondingly, the two peaks for Nb 3d centered at 206.7 eV and 209.5 eV of $MnNb_2O_6$ also shifted toward the lower binding energy at about 206.4 eV and 209.2 eV for the 5%NGQDs-Bi/Mn. These binding energy shifts in spectra could be attributed to the presence of strong interactions between BiOI and $MnNb_2O_6$. Additionally, the XPS signal of O 1s for 5% NGQDs-Bi/Mn photocatalyst was locating at 530.5 eV in Fig. 6f. The C 1s spectrum (Fig. 6g) in

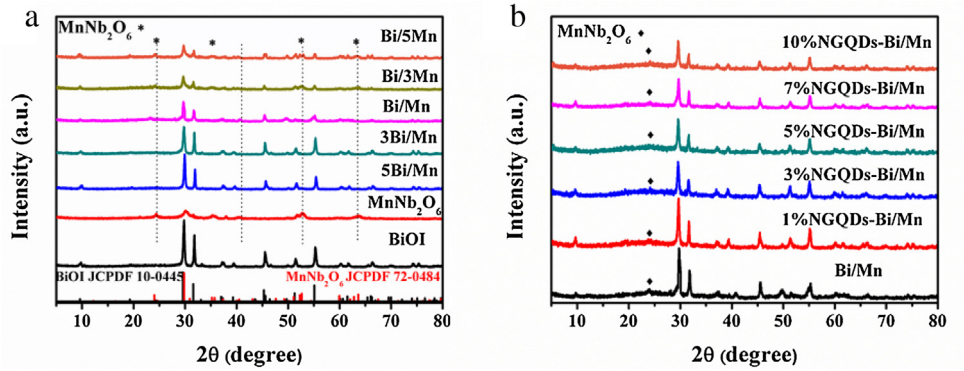

Fig. 1. XRD patterns of the as-prepared samples.

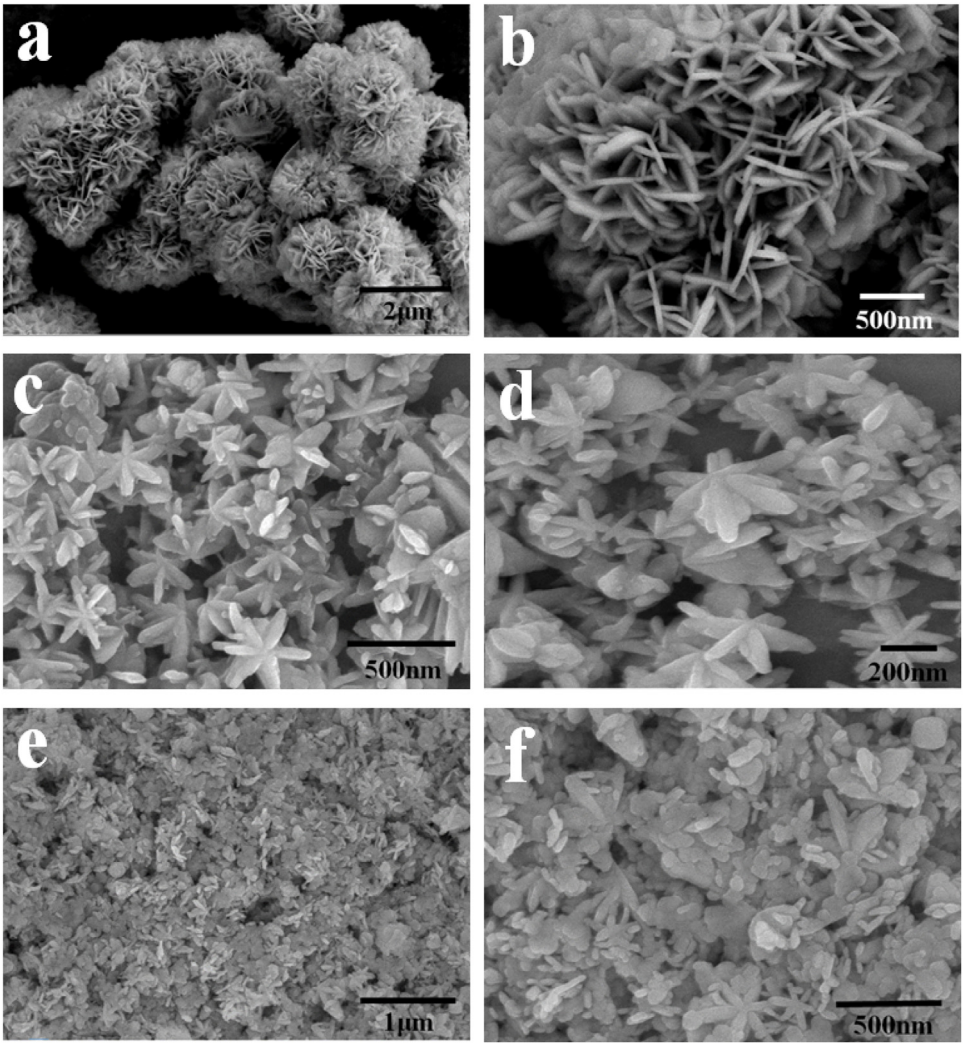

Fig. 2. SEM images of prepared samples BiOI (a–b), $MnNb_2O_6$ (c–d), 5%NGQDs- Bi/Mn (e–f).

the 5% NGQDs-Bi/Mn sample can be fitted into four peaks locate at 284.6, 285.2, 287.3 and 288.9 eV, which corresponded to C—C, C—N, C=O and O—C=O, respectively. The peak in N 1s spectrum located at 399.6 eV (Fig. 6h), which came from the NGQDs in the 5% NGQDs-Bi/Mn sample. The XPS results validated the coexistence of BiOI, $MnNb_2O_6$ and NGQDs in the 5% NGQDs-Bi/Mn photocatalysts, in addition, it also concluded that there was strong interfacial interaction between the BiOI and $MnNb_2O_6$, which could facilitate the transfer of photoinduced charge and improve the photocatalytic performance of 5% NGQDs-Bi/Mn immediately.

3.6. Photocatalytic behaviors

In this work, TC was chosen to evaluate the photocatalytic activity in Fig. 7a–b. Pure $MnNb_2O_6$ and BiOI showed weak activity, on which about only 7.2% and 30.5% of tetracycline were degraded under 60 min irradiation. With respect to the composites

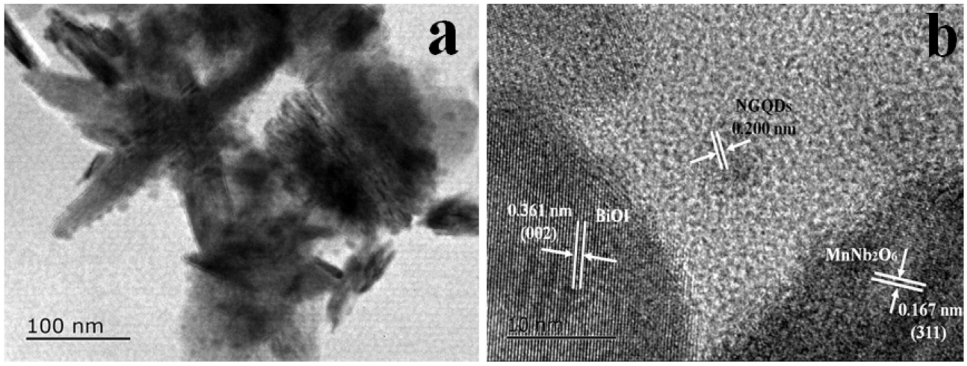

Fig. 3. TEM image (a) and HRTEM image of 5%NGQDs-Bi/Mn sample(b).

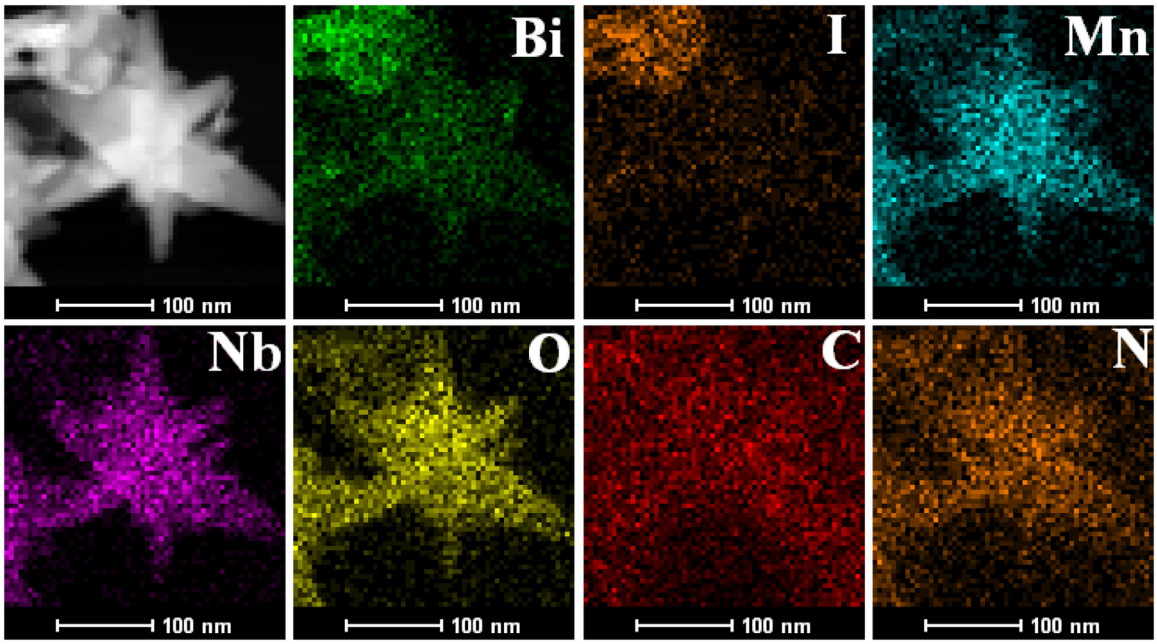

Fig. 4. HAADF-STEM images of the NGQDs- BiOI/$MnNb_2O_6$ composite.

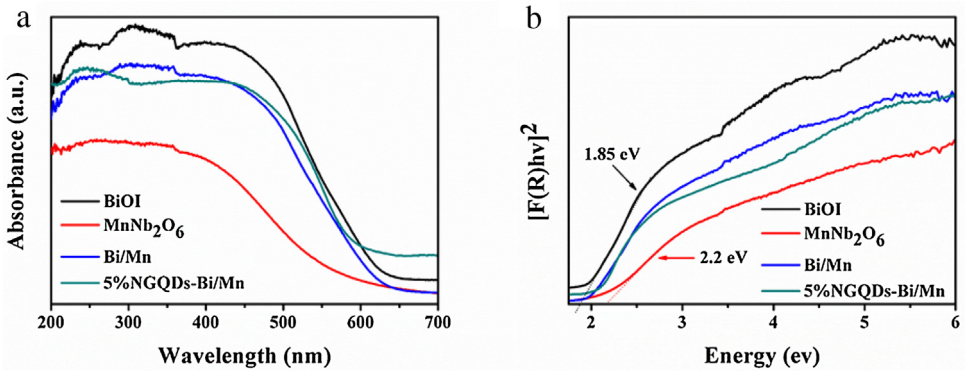

Fig. 5. UV–vis adsorption spectra (a) and calculated band gap (b) of prepared samples.

of BiOI/$MnNb_2O_6$, when the two semiconductors coupled together, it resulted in enhanced ability for the degradation. Among different proportionate samples, the Bi/Mn photocatalyst with the mole ratio of 1:1 exhibited the excellent activity about 71.3% within 60 min. However, if the BiOI or $MnNb_2O_6$ content exceeded to the 1:1 in the heterostructures, the photocatalytic activity would be decreased, which might be attribute to excessive BiOI and $MnNb_2O_6$ may act as the recombination center of electrons and holes to consequently restrain the photocatalytic activity [46]. After the modification of NGQDs onto the surface of the Bi/Mn, the photocatalytic activities can be significantly enhanced, which can be ascribed to the excellent electron transfer properties of NGQDs. Within 60 min irradiation, the tetracycline degradation ratio of the 5%NGQDs-Bi/Mn sample arrived 87.2%. However, when the NGQDs amount

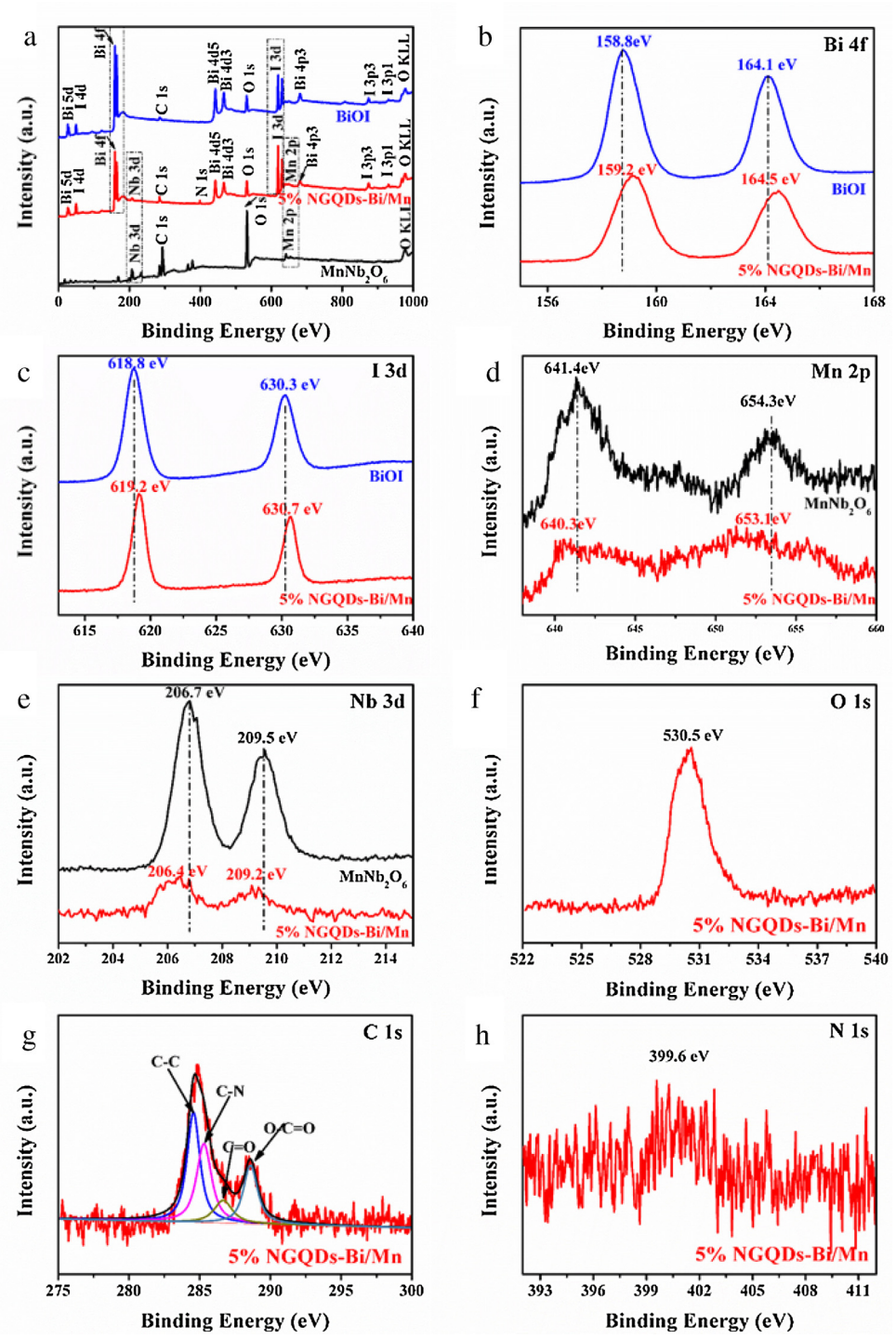

Fig. 6. XPS spectra of pure BiOI, $MnNb_2O_6$ and 5%NGQDs-Bi/Mn samples. Survey spectrum (a), Bi 4f (b), I 3d (c), Mn 2p (d), Nb 3d (e), O 1s (f), C1s (g) and N 1s (h).

was further increased from 5% to 10%, the TC degradation ratio would be decreased because of too many NGQD dispersed on the surface of Bi/Mn would shield the Bi/Mn from absorbing visible light. As is well known, the semiconductor needs to absorb light to generate charge carriers and then participate in the subsequent redox reactions. As a result, too much content of NGQD results in a decrease of photocatalytic performance.

The degradation kinetics of tetracycline by using the as-prepared samples were investigated and the results were exhibited in Fig. 7c–d. It can be observed that the changes of the tetracycline concentration vs the irradiation time over as-prepared samples conformed to the pseudo-first-order kinetics plot. The reaction rate constant (k) values were enhanced through the introduction of NGQDs. The 5%NGQDs-Bi/Mn sample (0.0331 min^{-1}) exhibited the highest k value among all the samples, which was about 27.6-fold and 5.6-fold higher than that of pure $MnNb_2O_6$ (0.0012 min^{-1}) and BiOI (0.0059 min^{-1}).

As broad-spectrum antibiotic agent, oxytetracyline, ciprofloxacin and doxycycline were also selected as the target pollutants for photodegradation to acquire better insight about the catalytic activities over the 5%NGQDs-Bi/Mn. As shown in Fig. 7e, under visible light irradiation for 120 min, 57.4%

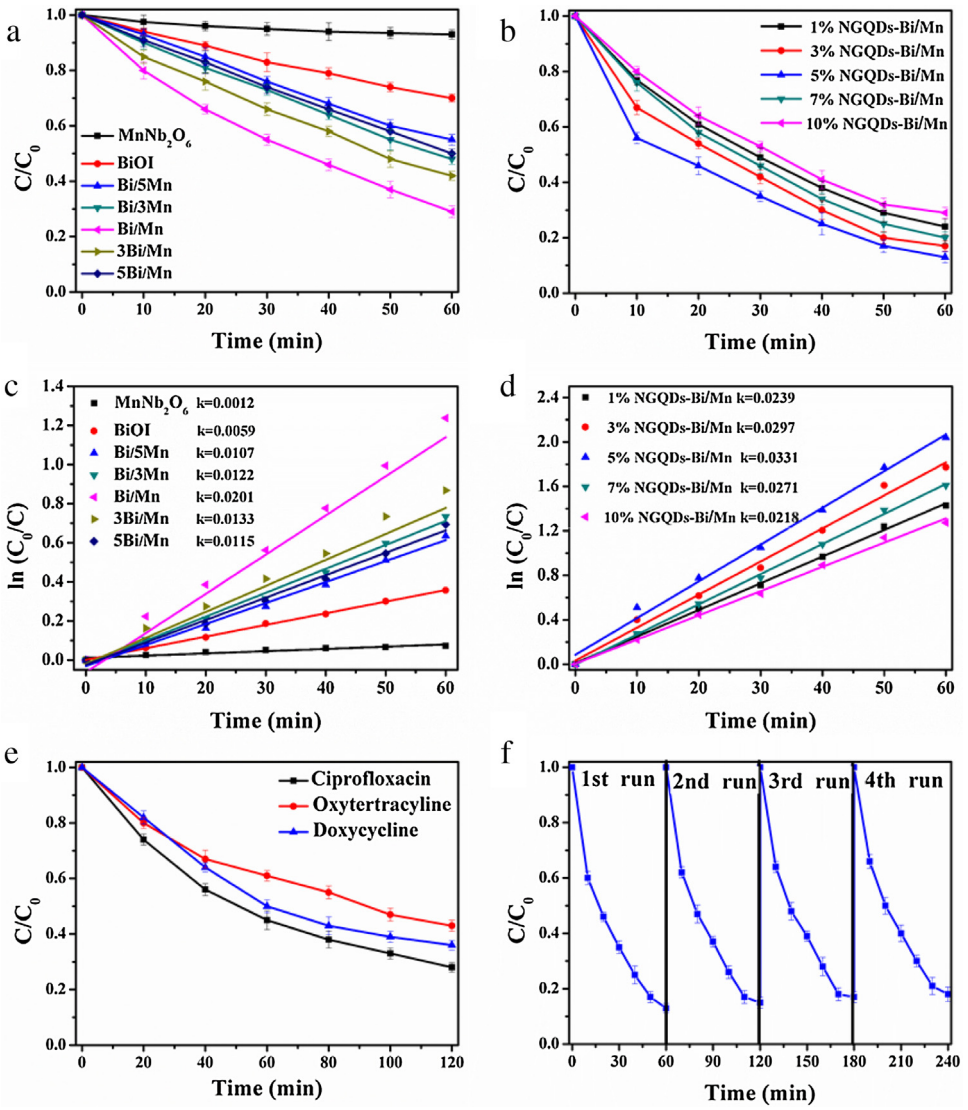

Fig. 7. Photocatalytic degradation of TC with as-prepared samples (a–b); the pseudo-first-order reaction kinetics for TC degradation with as-prepared samples (c–d); photocatalytic degradation of other antibiotics with 5%NGQDs-Bi/Mn sample (e); four cycling experiments of 5%NGQDs-Bi/Mn for TC degradation (f).

ciprofloxacin, 64.7% doxycycline and 72.1% oxytetracyline could be degraded, suggesting that the 5%NGQDs-Bi/Mn sample was an efficient photocatalyst for the antibiotic degradation.

The photocatalytic reusability and repeated performance of the 5%NGQDs-Bi/Mn sample were also studied by the repeating experiments of photocatalytic degradation TC. After each cycle, the photocatalyst was filtered and dried thoroughly, and then the fresh TC solution was added. After four successive recycles, the 5%NGQDs-Bi/Mn sample still maintain good photocatalytic stability under visible light in Fig. 7f. In addition, the XRD pattern after cycles was also provided in Fig. S2. After four cycles experiments, the characteristic peaks of the 5%NGQDs-Bi/Mn sample remain unchanged, which suggested that the sample was even stable after four cycles degradation processes.

3.7. The intermediates of TC degradation

The intermediates of TC during the photodegradation reaction under visible light were analyzed by HPLC–MS in Fig. S3. It is clearly observed that there was an intense prominent ion with m/z = 445 in Fig. S3a, which corresponded to TC. With increasing the reaction time, the intensity of TC peak at m/z = 445 became weak and other peaks with m/z values of 427, 410, 360, 292 and 164 increased gradually in Fig. S3b-d. On the basis of the conclusions of the experimental and the reported studies [47], the possible pathways of degradation were depicted in Fig. 8. At last, the intermediate products would be degraded to the CO_2, H_2O and some other small inorganic molecular materials.

3.8. Electrochemistry analysis and PL

Photocurrent and EIS were carried out to evaluate the kinetics of charge transfer with the BiOI, $MnNb_2O_6$, Bi/Mn and 5%NGQDs-Bi/Mn samples. Fig. 9a showed that the photocurrent increased rapidly when the light irradiation was activated. Meanwhile, after several cycles of intermittent on-off irradiation, the photocurrent was still keep steady and reproducible. The Bi/Mn composites exhibited a higher photocurrent response compared to pure $MnNb_2O_6$ and BiOI, indicating that when BiOI coupled with $MnNb_2O_6$ to form a p-n junction system, the separation ration of the photogenerated electrons and holes could be increased. However, when the Bi/Mn was modified with NGQDs, the photocurrent intensity became stronger, which could be attributed to the fact that the photogenerated electrons can be rapidly transfer from the

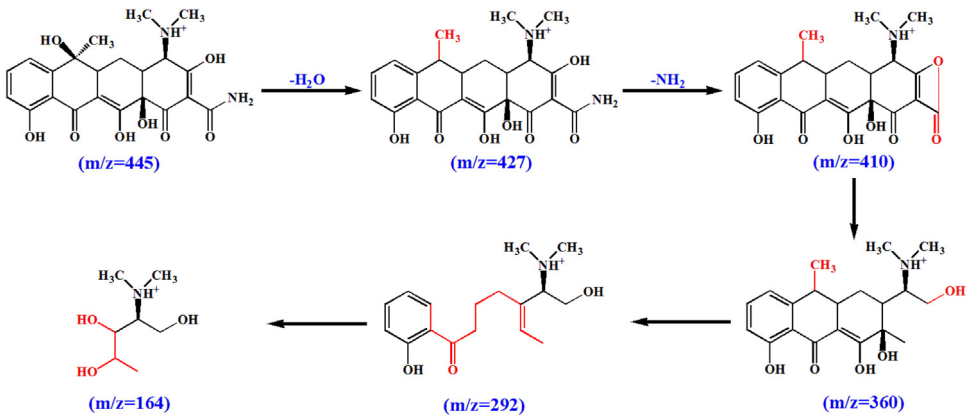

Fig. 8. Proposed degradation pathways for photocatalytic degradation of TC with 5%NGQDs- Bi/Mn sample.

CB to NGQDs, restricting the direct recombination of electrons and holes.

EIS was then carried out to explore the process of their charge transfer resistance. The radius of the arc about the EIS Nyquist plot represented the charge transfer rate occurring at the contact interface between the working electrode and electrolyte solution. The smaller radius of the Nyquist circle represented the lower charge-transfer resistance [48]. As shown in Fig. 9b, the 5%NGQDs-Bi/Mn sample displayed the smallest arc radius among all the samples, which indicated a faster interfacial charge transfer and a more effective separation of electron-hole appear in the p-n junction system by introducing of NGQDs.

In order to further verify the effect of the NGQDs, the photoluminescence (PL) measurements were carried out on the samples with Bi/Mn and 5%NGQDs-Bi/Mn. As we all known, PL analysis was applied to reveal the efficiency of charge carrier separation and transfer in semiconductors. In Fig. S4, the PL spectra of Bi/Mn and 5%NGQDs-Bi/Mn samples with an excitation wavelength at 360 nm. The emission intensity of 5%NGQDs-Bi/Mn was much lower than that of Bi/Mn, indicating that the NGQDs were benefit for separation and transfer of the charge carriers in the 5%NGQDs-Bi/Mn composite. Therefore, it can be speculated that the introduction of NGQDs can markedly improve photocatalytic performance. The conclusions were consistent with the photocurrents analysis and EIS.

3.9. Photocatalytic mechanism

To speculate the photocatalytic mechanism, species trapping experiments were carried out to capture the reactive species generated in the degradation process. From Fig. 10a–b, there was no obviously changes of photocatalytic efficiency when IPA was added to trap •OH. On the country, as the TEOA and BQ were injected into the solution to trap h^+ and $^{\bullet}O_2^-$, the photodegradation activity was slightly inhibited, which suggested that the $^{\bullet}O_2^-$ and h^+ radicals were the major reactive species in the reaction system.

The reactive species evolved in the process of photocatalytic reaction was investigated with the ESR technique by DMPO. It can be observed from Fig. 10c, the six characteristic peaks of $^{\bullet}O_2^-$ existed in the spectra, which indicated that the photogenerated electrons in the conduction band of catalysts could be transformed into $^{\bullet}O_2^-$ radicals during the photo-degradation system. However, for the detection of •OH (Fig. 10d), there could be observed nearly no or a little characteristic peaks, suggesting nearly no •OH generated in the catalysts photocatalytic degradation system, which was consistent with results of the active species trapping experiment above.

In order to confirm the semiconductor types of BiOI and $MnNb_2O_6$, Mott-Schottky method was employed (Fig. 11a–b). It is well known that the slope of linear $1/C^2$ potential curves is positive for n-type semiconductor and negative for p-type semiconductor [49,50]. As shown in Fig. 11a–b, the slope of linear $1/C^2$ potential curve of BiOI and $MnNb_2O_6$ were separately negative and positive, suggesting that the BiOI was a p-type semiconductor and $MnNb_2O_6$ was a n-type semiconductor. The band edge positions of BiOI and $MnNb_2O_6$ were estimated in this study according to the electronegativity. The conduction band (CB) and valence band (VB) potentials of the two semiconductors can be evaluated by the formula according to the previous paper [11] as follows:

$$E_{CB} = X\text{-}E^e - 0.5E_g$$

$$E_{VB} = E_{CB} + E_g$$

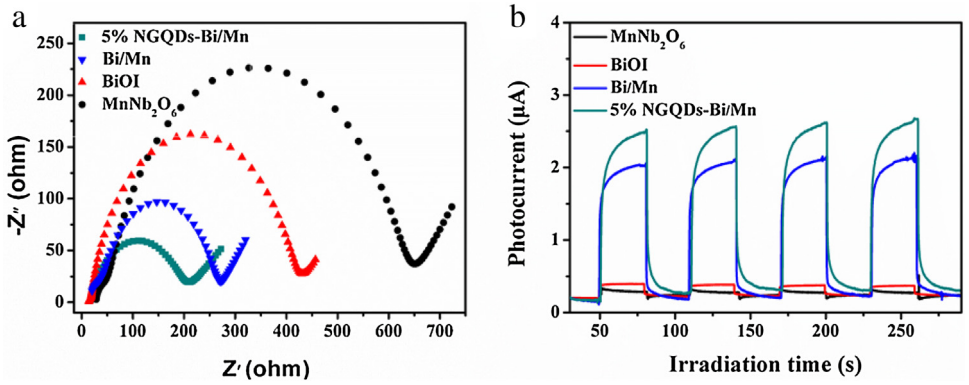

Fig. 9. EIS (a) and Transient photocurrent response (b) for the pure BiOI, $MnNb_2O_6$, Mn/Bi and 5%NGQDs-Bi/Mn samples.

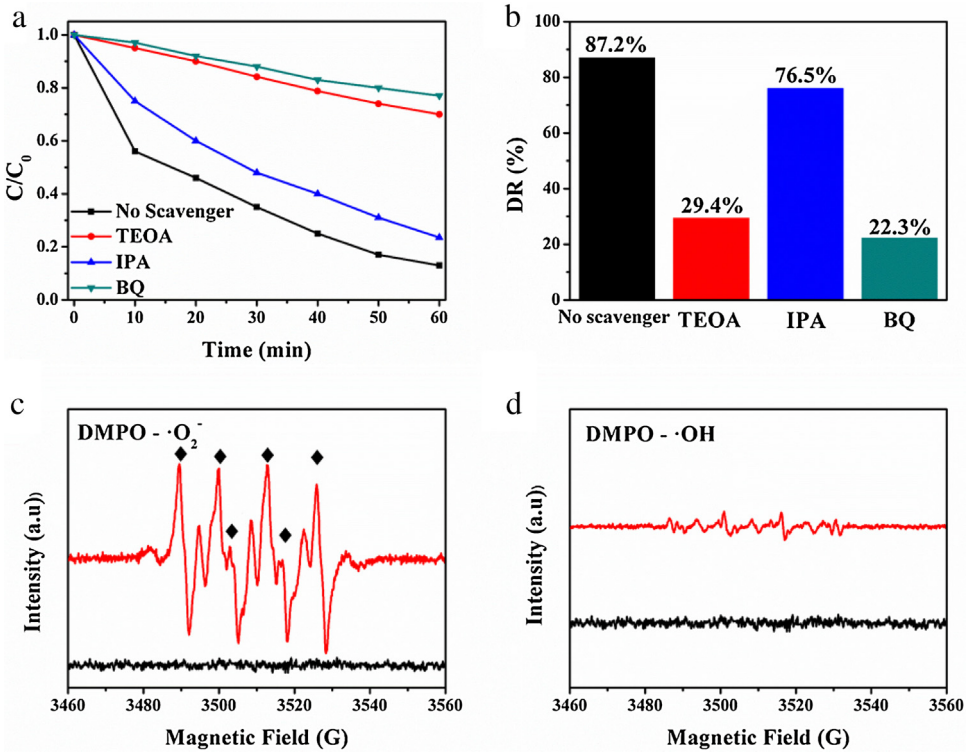

Fig. 10. The species trapping experiments for degradation of TC over 5%NGQDs- Bi/Mn photocatalyst under visible light irradiation (a–b); ESR spectra of 5%NGQDs-Mn/Bi samples for DMPO- $^{\bullet}O_2^-$ (c) and DMPO-$^{\bullet}$OH (d).

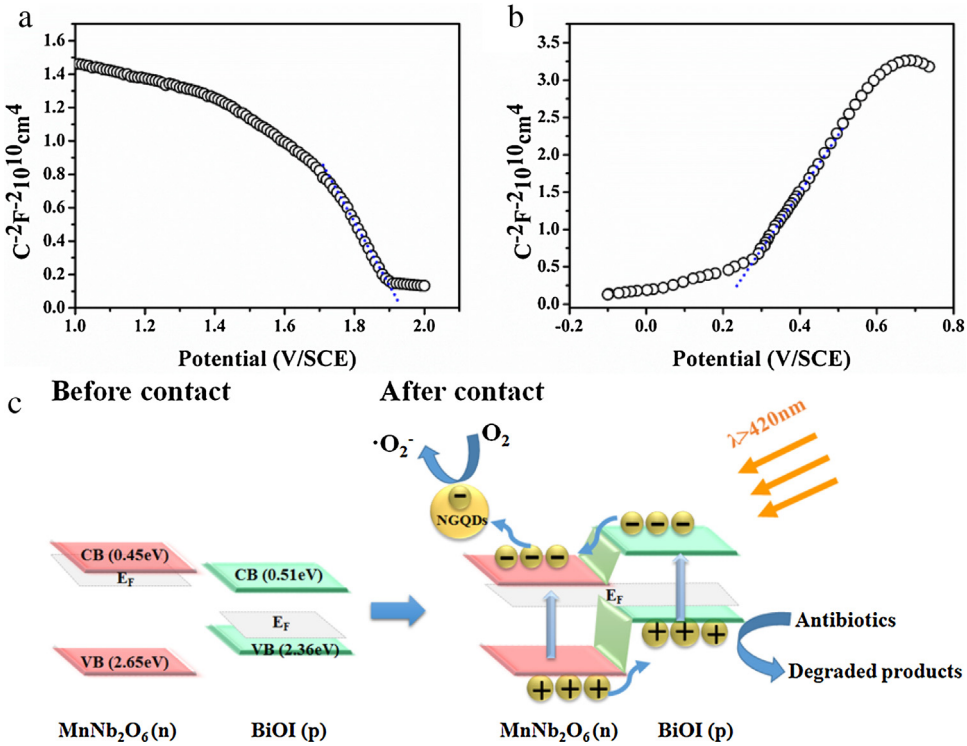

Fig. 11. Mott-Schottky curves of BiOI (a) and $MnNb_2O_6$ (b), schematic diagrams of formation of p-n junction and proposed charge separation process in the 5%NGQDs- Bi/Mn sample under visible-light irradiation (c).

where X is the electronegativity of the semiconductor (X value for BiOI is 5.94 and for $MnNb_2O_6$ is 6.05); E^e is the energy of free electrons on the hydrogen scale (4.5 eV). According to the UV–vis diffuse reflectance absorption spectra, the band gaps of BiOI and $MnNb_2O_6$ were1.85 eV and 2.2 eV, hence, the E_{VB} and E_{CB} of $MnNb_2O_6$ were calculated to be 2.65 eV and 0.45 eV, respectively, and those of BiOI are 2.36 eV and 0.51 eV, respectively.

According to the above experimental results on charge carrier behaviors and band energy levels, the schematic diagrams of the charge separation process on the 5%NGQDs-Bi/Mn p-n junction were displayed in Fig. 11c. Before contact, the $MnNb_2O_6$ and BiOI have the nested band structures, which were not benefit for efficient charge separation. As a p-type semiconductor, the Fermi level (E_F) of BiOI located close to valence band (VB), whereas $MnNb_2O_6$ is a n-type semiconductor with the E_F close to its conduction band (CB). After contacting to construct the BiOI/$MnNb_2O_6$ p-n heterojunction, the energy levels of BiOI moved up, while the energy levels of $MnNb_2O_6$ moved down until the E_F of BiOI and $MnNb_2O_6$ reach an equilibrium. As a result, the conduction band edge of BiOI was higher than that of $MnNb_2O_6$. At the equilibrium, the inner electric field was formed, thus the p-type BiOI region had the negative charge while n-type $MnNb_2O_6$ had the positive charge. Under visible-light irradiation, BiOI and $MnNb_2O_6$ could be easily excited and induced the generation of photoelectrons and holes, the excited e^- in the CB of BiOI can easily transfer to the CB of $MnNb_2O_6$. Simultaneously, holes on the $MnNb_2O_6$ VB can also inject into the BiOI VB. The migration of photogenerated carriers can be improved by the inner electric field established at the heterojunction interfaces. When the NGQDs was introduced, the e^- was accelerated to transfer, which would further improve the charge separation efficiency and therefore enhance the photocatalytic degradation activity.

4. Conclusion

In summary, a hydrothermal route was utilized to fabricate NGQDs-BiOI/$MnNb_2O_6$ p-n junction photocatalysts. The 5%NGQDs-Bi/Mn sample exhibited superior photocatalytic performance in the degradation of antibiotics than that of the pristine $MnNb_2O_6$ and BiOI. The enhanced photocatalytic activity under visible light irradiation can be ascribed to cooperative effects of p-n junction between the n-type $MnNb_2O_6$ and p-type BiOI and high charge carrier mobility of NGQDs, which greatly promoted efficient separation of the photoexcited electron-hole pairs as well as depressed the recombination of the charge carriers. Finally, the design principles outlined in this paper can be extended to other semiconductors to enhance the nanoscale heterostructures undergoing development for solar energy conversion.

Acknowledgements

The authors would like to acknowledge the National Natural Science Foundation of China (21276116, 21477050, 21301076, 21303074, 21522603 and 21576121), the Chinese-German Cooperation Research Project (GZ1091), the Excellent Youth Foundation of Jiangsu Scientific Committee (BK20140011), Natural Science Foundation of Jiangsu Province (BK20141304), Special Financial Grant from the China Postdoctoral (2015T80500), China Postdoctoral Science Foundation funded project (2014M551508), Program for New Century Excellent Talents in University (NCET-13-0835), the Henry Fok Education Foundation (141068), Six Talents Peak Project in Jiangsu Province (XCL-025) and Graduate Research and Innovation Program of Jiangsu University (KYXX_0022).

Appendix A. Supplementary data

Supplementary data associated with this article can be found, in the online version, at http://dx.doi.org/10.1016/j.apcatb.2016.09.039.

References

[1] L. Wollenberger, B. Halling-Sørensen, K.O. Kusk, Chemosphere 40 (2000) 723–730.
[2] J.L. Martinez, Environ. Pollut. 157 (2009) 2893–2902.
[3] A.K. Sarmah, M.T. Meyer, A.B. Boxall, Chemosphere 65 (2006) 725–759.
[4] G. Hamscher, S. Sczesny, H. Hoper, H. Nau, Anal. Chem. 74 (2002) 1509–1518.
[5] L. Zhao, Y.H. Dong, H. Wang, Sci. Total Environ. 408 (2010) 1069–1075.
[6] A. Kubacka, M. Fernandez-Garcia, Chem. Rev. 112 (2012) 1555–1614.
[7] X.B. Chen, S.H. Shen, L.J. Guo, S.S. Mao, Chem. Rev. 110 (2010) 6503–6570.
[8] N. Zhang, M.Q. Yang, S.Q. Liu, Y.G. Sun, Y.J. Xu, Chem. Rev. 115 (2015) 10307–10377.
[9] Y. Ma, X.L. Wang, Y.S. Jia, X.B. Chen, H.X. Han, C. Li, Chem. Rev. 114 (2014) 9987–10043.
[10] Q. Han, B. Wang, Y. Zhao, C.G. Hu, L.T. Qu, Angew. Chem. Int. Ed. 54 (2015) 11433–11437.
[11] S.M. Wang, D.L. Li, C. Sun, S.G. Yang, Y. Guan, H. He, Appl. Catal. B 144 (2014) 885–892.
[12] S.M. Sun, W.Z. Wang, D.Z. Li, L. Zhang, D. Jiang, ACS Catal. 4 (2014) 3498–3503.
[13] Y. Yan, Y.F. Wu, Y.T. Yan, W.D. Guan, W.D. Shi, J. Phys. Chem. C 117 (2013) 20017–20028.
[14] Y.C. Huang, W.J. W, B. Long, H.B. Li, F.Y. Zhao, Z.L. Liu, Y.X. Tong, H.B. Ji, Appl. Catal. B 185 (2016) 68–76.
[15] Y.C. Huang, B. Long, H.B. Li, M.S. Balogun, Z.B. Rui, Y.X. Tong, H.B. Ji, Adv. Mater. Interfaces 2 (2015) 1500249.
[16] J. Di, J.X. Xia, Y.P. Ge, L. Xu, H. Xu, M.Q. He, Q. Zhang, H.M. Li, J. Mater. Chem. A 2 (2014) 15864–15874.
[17] H.W. Huang, Y. He, X. Du, P.K. Chu, Y.H. Zhang, ACS Sustainable Chem. Eng. 3 (2015) 3262–3273.
[18] C.L. Yu, J.C. Yu, C.F. Fan, H.R. Wen, S.J. Hu, Mater. Sci. Eng. 166 (2010) 213–219.
[19] H. Liu, W.R. Cao, Y. Su, Y. Wang, X.H. Wang, Appl. Catal. B 111 (2012) 271–279.
[20] T.B. Li, G. Chen, C. Zhou, Z.Y. Shen, R.C. Jin, J.X. Sun, Dalton Trans. 40 (2011) 6751–6758.
[21] Y. Zhang, Q. Pei, J.C. Liang, T. Feng, X. Zhou, H. Mao, W. Zhang, Y. Hisaeda, X.M. Song, Langmuir 31 (2015) 10279–10284.
[22] Y.C. Huang, H.B. Li, M.S. Balogun, W.Y. Liu, Y.X. Tong, X.H. Lu, H.B. Ji, ACS Appl. Mater. Interfaces 6 (2014) 22920–22927.
[23] B. Long, Y.C. Huang, H.B. Li, F.Y. Zhao, Z.B. Rui, Z.L. Liu, Y.X. Tong, H.B. Ji, Ind. Eng. Chem. Res. 54 (2015) 12788–12794.
[24] W.J. Fan, H.B. Li, F.Y. Zhao, X.J. Xiao, Y.C. Huang, H.B. Ji, Y.X. Tong, Chem. Commun. 52 (2016) 5316–5319.
[25] B. Hu, F.P. Cai, H. Shen, M.S. Fan, X. Yan, W.Q. Fan, L.S. Xiao, W.D. Shi, CrystEngComm 16 (2014) 9255–9265.
[26] D.Y. Pan, J.C. Zhang, Z. Li, M.H. Wu, Adv. Mater. 22 (2010) 734–738.
[27] L.L. Li, J. Ji, R. Fei, C.Z. Wang, Q. Lu, J.R. Zhang, Adv. Funct. Mater. 22 (2012) 2971–2979.
[28] D. Qu, M. Zheng, P. Du, Y. Zhou, L.G. Zhang, D. Li, Nanoscale 5 (2013) 12272–12277.
[29] J.Y. Ji, J.L. Liu, L.F. Lai, X. Zhao, Y.D. Zhen, J.Y. Lin, ACS Nano 9 (2015) 8609–8616.
[30] P. Chen, T.Y. Xiao, H.H. Li, J.J. Yang, Z. Wang, H.B. Yao, ACS Nano 6 (2012) 712–719.
[31] L.M. He, L.Q. Jing, Y.B. Luan, L. Wang, H.G. Fu, ACS Catal. 4 (2014) 990–998.
[32] D. Jiang, Q. Liu, K. Wang, J. Qian, Y.Y. Dong, Z.T. Yang, Biosens. Bioelectron. 54 (2014) 273–278.
[33] Y. Li, Y. Zhao, H.H. Cheng, Y. Hu, G.Q. Shi, L.M. Dai, J. Am. Chem. Soc. 134 (2012) 15–18.
[34] S. Dey, A. Govindaraj, K. Biswas, C. Rao, Chem. Phys. Lett. 595 (2014) 203–208.
[35] L.B. Tang, R.B. Ji, X.M. Li, K.S. Teng, S.P. Lau, J. Mater. Chem. C 1 (2013) 4908–4915.
[36] Q.Q. Li, S. Zhang, L.M. Dai, L.S. Li, J. Am. Chem. Soc. 134 (2012) 18932–18935.
[37] X.J. Du, D. Jiang, Q. Liu, G.B. Zhu, H.P. Mao, K. Wang, Analyst 140 (2015) 1253–1259.
[38] Y.Y. Yin, Q. Liu, D. Jiang, X.J. Du, J. Qian, H.P. Mao, K. Wang, Carbon 96 (2016) 1157–1165.
[39] Z. Yang, M.H. Xu, Y. Liu, F.J. He, F. Gao, Y.J. Su, Nanoscale 6 (2014) 1890–1895.
[40] Q.H. Liang, W.J. Ma, Y. Shi, Z. Li, X.M. Yang, Carbon 60 (2013) 421–428.
[41] H.B. Wang, T. Maiyalagan, X. Wang, ACS Catal. 2 (2012) 781–794.
[42] F. Wang, M. Kreiter, B. He, S.P. Pang, C.Y. Liu, Chem. Commun. 46 (2010) 3309–3311.
[43] J. Di, J.X. Xia, M.X. Ji, B. Wang, X.W. Li, Q. Zhang, Z.G. Chen, H.M. Li, ACS Sustainable Chem. Eng. 4 (2016) 136–146.
[44] J. Di, J.X. Xia, M.X. Ji, X. Li, Z.G. Chen, H.M. Li, J. Mater. Chem. A 4 (2016) 5051–5061.
[45] J. Di, J.X. Xia, Y.P. Ge, H.P. Li, H.Y. Ji, H. Xu, Q. Zhang, H.M. Li, M.N. Li, Appl. Catal. B 168 (2015) 51–61.
[46] Z.Y. Zhang, D.L. Jiang, D. Li, M.Q. He, M. Chen, Appl. Catal. B 183 (2016) 113–123.
[47] M.J. Zhou, J.Z. Li, Z.F. Ye, C.C. Ma, H.Q. Wang, P.W. Huo, W.D. Shi, Y.S. Yan, ACS Appl. Mater. Interfaces 7 (2015) 28231–28243.
[48] J. Di, J.X. Xia, S. Yin, H. Xu, L. Xu, Y.G. Xu, M.Q. He, H.M. Li, J. Mater. Chem. A 2 (2014) 5340–5351.
[49] G.G. Liu, T. Wang, S.X. Ouyang, L.Q. Liu, H.Y. Jiang, Q. Yu, T. Kako, J.H. Ye, J. Mater. Chem. A 3 (2015) 8123–8132.
[50] Z.Q. He, D. Wang, H.Y. Fang, J.M. Chen, S. Song, Nanoscale 6 (2014) 10540–10544.